



Enhancement of the photocatalytic activity and white emission of CaIn_2O_4 nanocrystals



M.T.S. Tavares^a, M.M. Melo^b, V.D. Araújo^c, R.L. Tranquilin^d, C.R.R. Almeida^d,
C.A. Paskocimas^d, M.R.D. Bomio^d, E. Longo^{e,*}, F.V. Motta^d

^a IFBA, Campus Feira de Santana, CEP 44096-486 Bahia, BA, Brazil

^b IFRN, Campus Santa Cruz, CEP 59200-000 Santa Cruz, RN, Brazil

^c UACSA – UFRPE, Recife, CEP 52171-900 Recife, PE, Brazil

^d LSQM- Laboratório de Síntese Química de Materiais, DEMAT, UFRN, Natal, Campus Lagoa Nova, CEP 59078-900 Natal, RN, Brazil

^e LIEC- Laboratório interdisciplinar de eletroquímica e cerâmica – DQ, UFSCar, CEP 13565-905 São Carlos, SP, Brazil

ARTICLE INFO

Article history:

Received 21 August 2015

Received in revised form

3 October 2015

Accepted 18 October 2015

Available online 27 October 2015

Keywords:

CaIn_2O_4

Ultrasonic spray pyrolysis

Nanocrystals

Photocatalysis

Photoluminescence

White-light

ABSTRACT

CaIn_2O_4 (CIO) nanocrystals (NCs) were prepared by ultrasonic spray pyrolysis at 1223 K without the use of surfactants to investigate the influences of the nanostructure on the photoluminescence and photocatalytic properties of this white-light emitter. The optical properties were analyzed by ultraviolet–visible (UV–vis) absorption spectroscopy, which indicated a band gap energy of 3.83 eV, and photoluminescence (PL) measurements at room temperature that showed a broad and intense emission band. X-ray diffraction (XRD) analysis confirmed that the CIO NCs adopted the orthorhombic crystalline phase. Field-emission gun scanning electron microscopy (FEG-SEM) micrographs demonstrated the spherical morphology of the CIO NCs, comprising aggregates of several CIO NCs. Furthermore, the as-synthesized CIO NCs exhibited enhanced activity for the photodegradation of methylene blue (MB) under UV–vis irradiation. The chromaticity coordinates were calculated for the sample based on the PL spectrum; the CIO NCs had values of $x = 0.31$ and $y = 0.38$, and this point is located on the white region of the CIE diagram. Ultrasonic spray pyrolysis provides a feasible approach for preparing shape- and size-controlled CIO nanocrystals that hold great potential for photocatalytic applications and as photoluminescent white emitters.

© 2015 Elsevier B.V. All rights reserved.

1. Introduction

Recently, the design and production of new materials with controlled optical properties, such as semiconductor nanocrystals, have been intensively studied [1–3]. Indium-based oxides have attracted increasing attention in the last few years because their properties are potentially exploitable in optoelectronic devices, biological applications, catalysis, and other technologies [4–9]. CaIn_2O_4 (CIO) is a compound belonging to the AB_2X_4 family. According to the literature, CaIn_2O_4 shows potential for the degradation of organic pollutants and is an eco-friendly material [8,10].

Conventionally, the synthesis of CIO particles requires high temperatures and long synthesis or calcination times. Zeng et al. [11] synthesized CaIn_2O_4 by calcination at high temperatures of

1073 and 1323 K over long periods of 1 and 12 h, respectively. CIO photocatalysts have been obtained by solid–state reaction [12–16] and solution–combustion methods [17] that involved high temperatures and calcination times varying from 12 to 24 h. In order to minimize these inconveniences, other synthetic routes have been developed to obtain CIO, such as solvothermal [8], co-precipitation [18,19], sol–gel [20–22], and an optimized solid–state reaction [7].

It is known that the key factors controlling photocatalytic reactions are the efficiency of (1) adsorption of the reactant on the surface of the material and (2) light absorption by the material, as well as migration of the light-induced electrons and holes. The former is strongly dependent on the surface area of the material and the latter is related to the electronic structure characteristics of the material [16]. Based on these trends, the development of new strategies to obtain CIO NC photocatalysts with high surface area and optimum electronic properties geared toward photocatalysis is of great importance.

Ultrasonic spray pyrolysis is deemed an effective technique for

* Corresponding author.

E-mail address: elson.liec@gmail.com (E. Longo).

powder production using short production times and for generating a homogenous particle composition in a single-step, and is a continuous process that facilitates control of the mean particle size; furthermore, the purity of the products is high and the composition of the powders is easily controlled. Moreover, the powder particles achieved with this process are spherical and non-agglomerated [23,24]. In this study, we report the synthesis of CIO NCs with microspherical morphology, which were prepared by ultrasonic spray pyrolysis. We also show that by obtaining a material with a well-defined morphology, the photocatalytic efficiency towards MB degradation is enhanced in comparison with the reported properties for the same material. A chromaticity diagram is also constructed from the emission spectral data to verify the efficiency of CIO NCs as white-light emitters.

2. Experimental

2.1. Materials

Indium nitrate ($\text{In}(\text{NO}_3)_3 \cdot \text{H}_2\text{O}$, 99.9% purity; Alfa Aesar), calcium nitrate ($\text{Ca}(\text{NO}_3)_2 \cdot 4\text{H}_2\text{O}$, 99% purity; Synth), and distilled water were used as received to prepare the CIO NCs.

2.2. Preparation of CaIn_2O_4 nanocrystals

The CIO NCs were obtained by ultrasonic spray pyrolysis [25]. The precursor solution was prepared by dissolving 0.045 mol of $\text{Ca}(\text{NO}_3)_2 \cdot 4\text{H}_2\text{O}$ and 0.09 mol of $\text{In}(\text{NO}_3)_3 \cdot \text{H}_2\text{O}$ in 100 mL of distilled water. Fig. 1 shows a schematic of the spray pyrolysis system. The droplet generator comprised an ultrasonic nebulizer (HUMIDAIR PETIT). The laminar flow aerosol reactor used in the present study was a quartz tube of 37 mm inner diameter and 1.86 m length, which was inserted into a horizontal electric furnace. The precursor solution was atomized at a frequency of 2.4 MHz by using the ultrasonic nebulizer. The sprayed droplets were carried to the reactor, heated by the electric furnace at 1223 K in air, and converted into solid oxide particles within the laminar flow aerosol reactor. The resulting particles were collected at the reactor exit by the electrostatic precipitator. The overall flow rate of air used as a carrier gas was 2 L min^{-1} . If we assume plug flow in the reactor, the corresponding residence time of the particles inside the reactor was approximately 1 min.

2.3. Characterization of CaIn_2O_4 nanocrystals

The CIO NCs were structurally characterized by XRD using a Shimadzu XRD 7000 instrument with $\text{Cu-K}\alpha$ radiation

($\lambda = 1.5406 \text{ \AA}$) in the 2θ range from 10° to 80° at a scanning rate of $0.02^\circ \text{ s}^{-1}$. The morphologies were investigated using field-emission gun scanning electron microscopy (FEG-SEM; Carl Zeiss, Supra 35-VP Model, Germany) operated at 6 kV. Nitrogen adsorption/desorption isotherms and the specific surface areas were recorded with a Belsorp Mini instrument, Bel Japan. In addition, the BET method (Brunauer, Emmett, and Teller) was employed to estimate the specific surface area. The UV–vis diffuse reflectance spectrum was measured at room temperature using a UV–vis spectrometer. The photocatalytic activity of the CIO NCs (as catalyst agents) for the degradation of methylene blue (MB; $[\text{C}_{16}\text{H}_{18}\text{ClN}_3\text{S}]$; 99.5% purity, Mallinckrodt) in an aqueous solution was evaluated under UV irradiation. About 50 mg of catalyst crystals was placed in a 250-mL beaker and 50 mL of MB solution ($1 \times 10^{-5} \text{ mol L}^{-1}$) was added at $\text{pH} = 4$. The suspension was ultrasonicated for 10 min in an ultrasonic cleaner before irradiation and was then stored in the dark for 2 h to allow saturation of the catalyst by MB. The beakers were then placed in a photo-reactor at 25°C and were irradiated using six UV lamps (TUV Philips, 15 W with maximum intensity at 254 nm). The light power was measured (Coherent Power Max No PM10 Model), where the optical energy density value was 20 mW cm^{-2} . At ten-minute intervals, a 3-mL aliquot of the suspension was removed and centrifuged at 9000 rpm for 5 min to remove crystals in the suspension. Finally, the variations of the maximum absorption band of the supernatant solutions were monitored by UV–visible absorbance spectral measurements using a Shimadzu (model UV-2600) spectrophotometer. Photoluminescence (PL) spectra were acquired with an Ash Monospec 27 monochromator (Thermal Jarrel, U.S.A.) and a R4446 photomultiplier (Hamamatsu Photonics, U.S.A.). The 350 nm beam of a krypton ion laser (Coherent Innova 90 K) was used as the excitation source while maintaining its maximum output power at 200 mW. All measurements were performed at room temperature.

3. Results and discussion

The as-prepared CIO NCs were characterized by field-emission scanning electron microscopy (FEG-SEM), as shown in Fig. 2a and b. The inset in Fig. 2a presents the mean width distribution, which was estimated based on measurements of at least 300 microspheres in the FEG-SEM images and by fitting the resulting distribution using a Gaussian function.

The FEG-SEM images showed that the CaIn_2O_4 microspheres were composed mainly of nanoparticles with an average diameter of 511 nm. Fig. 2b shows that a few of the nanocrystals present irregular morphology, related to the final step of the formation process presented below. The XRD patterns of the samples (Fig. 3)

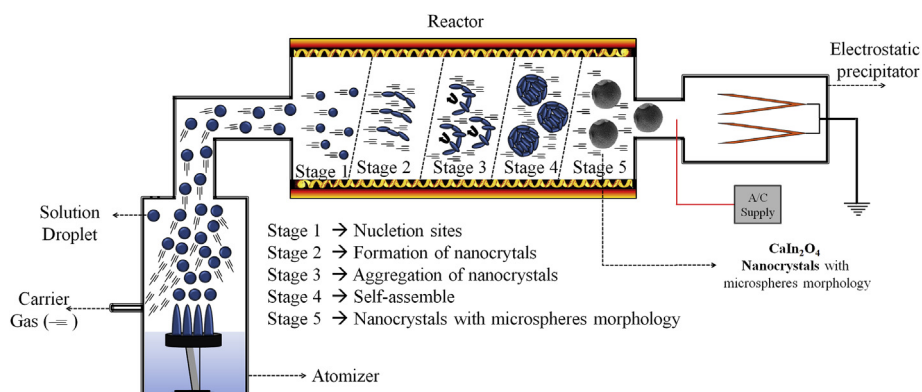


Fig. 1. Schematic of the experimental apparatus and the formation of CaIn_2O_4 nanocrystals obtained by one-pot ultrasonic spray pyrolysis.

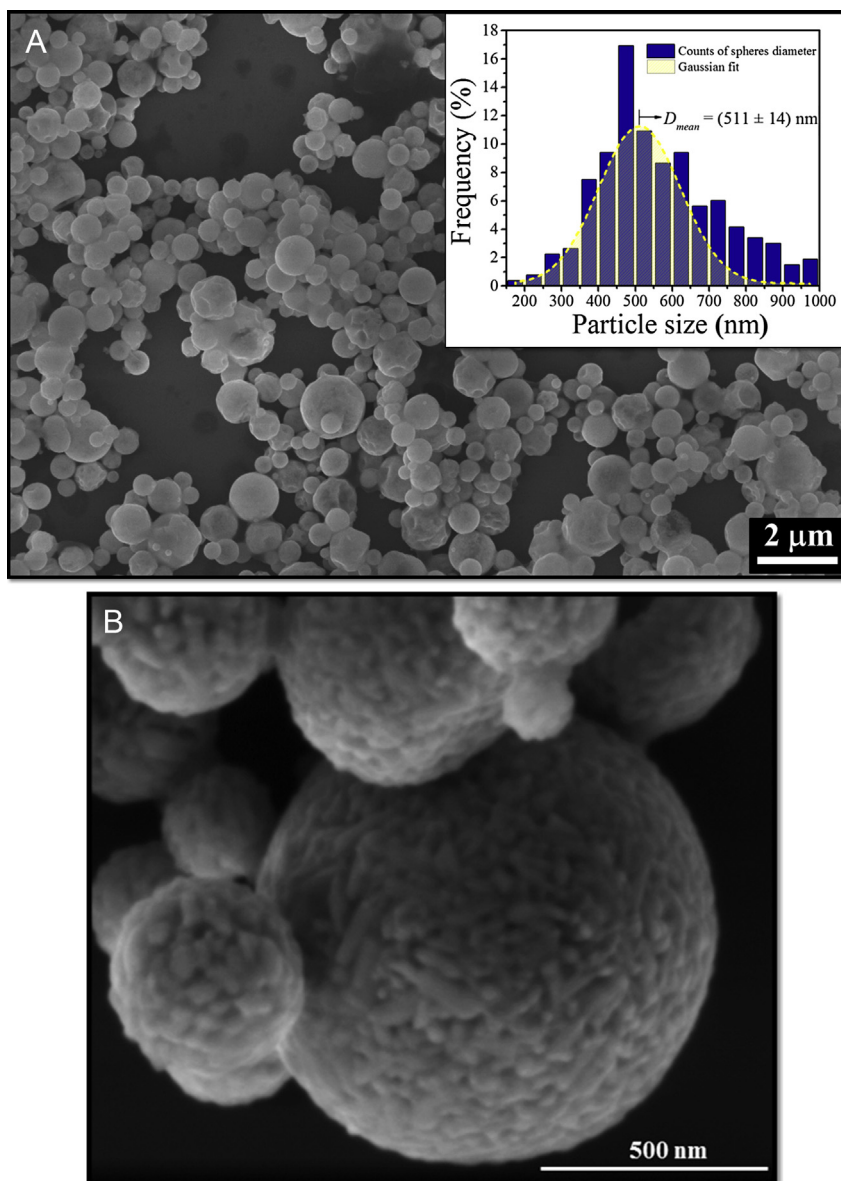


Fig. 2. (a) FEG-SEM images of ClO NCs obtained by one-pot ultrasonic spray pyrolysis. Inset in Figure 2a shows particle size distribution. (b) Microsphere composed by ClO NCs.

showed that the ClO NCs are structurally related to the orthorhombic CaIn_2O_4 crystalline phase (JCPDS card no. 17–643) [26]. A small percentage (estimated to be <2%) of secondary phase peaks was found, which is related to $\text{Ca}_9\text{Cu}_2\text{In}_{14}\text{O}_{32}$ (JCPDS card no. 48–695), originating from interaction of the ClO NCs with the copper plates from the electrostatic precipitator. Table 1 summarizes the lattice parameters a , b , c , and e , and the unit cell volume (V) and crystallite size (D) for the CaIn_2O_4 samples.

Fig. 4 presents a schematic of all the stages involved in the synthesis and growth of CaIn_2O_4 nanocrystals processed in the reactor (Fig. 1). Firstly, stoichiometric quantities of the $\text{Ca}(\text{NO}_3)_2 \cdot 4\text{H}_2\text{O}$ and $\text{In}(\text{NO}_3)_3 \cdot \text{H}_2\text{O}$ precursors were separately dissolved in one tube containing 100 mL of deionized water. In this solution, the solvation energy of H_2O molecules causes fast dissociation of the reagents, i.e., the Ca^{2+} and In^{3+} ions are solvated by the H_2O and NO_3^- species. It is well known that the Ca atoms coordinate with four H_2O and two NO_3^- , and In atoms coordinate with three NO_3^- and two H_2O to form distorted octahedral $\text{Ca}(\text{H}_2\text{O})_4(\text{NO}_3)_2$ and $\text{In}(\text{H}_2\text{O})_2(\text{NO}_3)_3$ clusters (Fig. 4). The partial negative charges of

these cluster complexes are electrostatically attracted by the Ca clusters, while the positive charges of the Ca clusters attract the In clusters. Due to the difference in the electronic density of the Ca and In cluster complexes, there is a strong electrostatic attraction between them. Upon evaporation of the solvent, the viscosity of water decreases and the mobility of the cluster complex is then favored, considerably increasing the effective rate of collisions between the species in solution. Moreover, thermal decomposition (Fig. 1—stage 1) occurs directly in the nucleation sites, forcing the crystallization kinetics of the primary crystals. As these nuclei have free rotation, collide at random, and can rearrange in relation to each other through motion, nanocrystals are effectively generated (Fig. 1—stages 2 and 3).

Smaller nanocrystals tend to undergo self-assembly (Fig. 1—stage 4), possibly via Van der Waals [27] interactions, in order to achieve the minimum energy per volume ratio [28]. Besides favoring the growth kinetics of the nanocrystals, thermal decomposition may favor heterogeneous nucleation and aggregation of the nanocrystals.

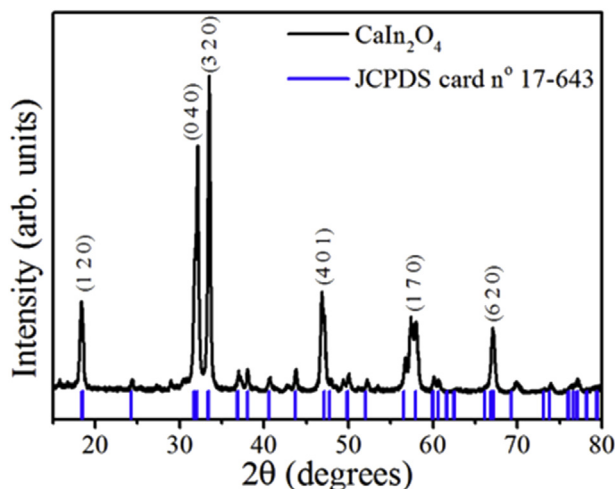


Fig. 3. XRD patterns of CIO NCs obtained by one-pot ultrasonic spray pyrolysis.

Table 1

Lattice constants (a , b and c), FWHM, cell volume (V) and the average crystallite size (D) of the cubic structure of CaIn_2O_4 powders prepared by one-pot ultrasonic spray pyrolysis.

a (Å) ^a	b (Å) ^a	c (Å) ^a	FWHM ^a	$V(\text{Å}^3)$ ^a	$D(\text{nm})$ ^a
11.663	10.527	3.887	0.1378	477.245	3.02

^a Calculated using the (320) 100% diffraction peak.

Fig. 1—stage 5 shows the proposed growth mechanism responsible for formation and growth of the aggregated CaIn_2O_4 nanocrystals. The high drying temperature can produce incremental temperature differences between the outer surface of the wet nanoparticles and the wet core, which will in turn lead to thermal stresses in the crystals.

Thus, after formation of the first nuclei, self-organization and/or mutual aggregation occurs between the nuclei by uncountable

collision events. The self-assembly mechanism is controlled by nanocrystal–nanocrystal interactions followed by coalescence. The growth and agglomeration of these nanocrystals are the origin of the complex superstructures with the formation of microspheres.

In these superstructures, there are strong bonds between the [... O–In–O ...] and neighboring [... Ca–O–Ca ...] clusters, where the internal/external vibrational spectra provide information on the structure and degree of order–disorder in the lattice [29–31].

The symmetry breaking in these nanocrystals can arise from different factors, such as distortions of the $[\text{InO}_6]$ clusters, modifications of the O–In–O bond lengths, changes in the dihedral angles, and formation of oxygen vacancies. It is well established that the effects of structural order–disorder occur over the short, medium, or long range [29]. Therefore, these kinds of structural defects modify the electronic band structure of the CIO NC, thereby affecting its properties.

Notably, many researchers have dealt with modeling the process for drying sprayed particles [32–35], where it was shown that high drying temperatures could produce steep temperature differences between the outer surface of the wet particle and the wet core, in turn leading to thermal stresses in the particle crust. The thermal stresses can cause particle cracking/rupture depending on the granule diameter, drying agent temperature, and the diameter of the primary colloidal particles. Thus, the irregular morphology observed for some particles (Fig. 1) may be due to thermal stresses during the drying step.

The PL spectrum of the CIO NCs prepared by the spray pyrolysis method is shown in Fig. 5a. The inset in Fig. 5a presents the white light emission under $\lambda_{\text{EX}} 350.7 \text{ nm}$. The results show a broadband emission covering a large part of the visible spectrum (400–800 nm) for the CIO NCs. The photoluminescence spectra indicate a typical multi-phonon process, i.e., there are various levels of decay resulting in the formation of a broad energy band [36]. According to the Gaussian line broadening mechanism for luminescence processes, the fine features in the PL spectrum of the CIO NCs were deconvoluted and extracted from the deconvolution curves [36]. Fig. 5a illustrates such decompositions, with the areas (percentages) under the curve of the respective transitions. The PL

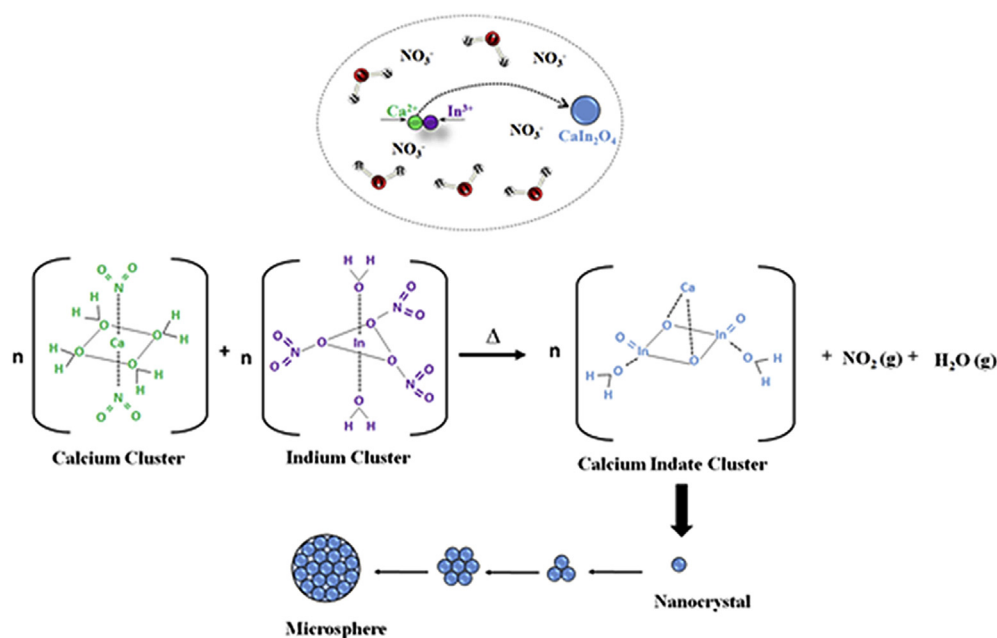


Fig. 4. Schematic representation of the synthesis and growth mechanisms for CIO NCs.

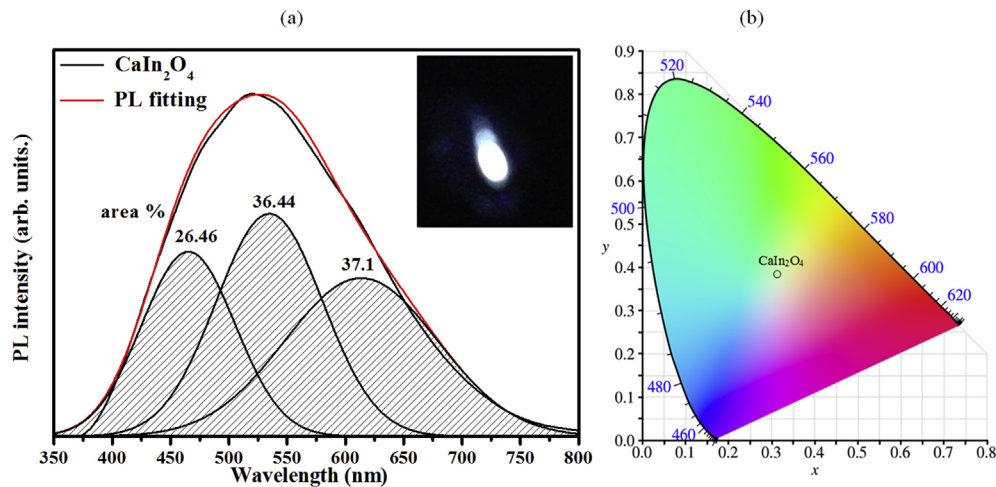


Fig. 5. (a) PL spectrum of CIO NC powders obtained by ultrasonic spray pyrolysis at 1223 K and deconvolution curve (area (%): obtained by dividing the area of each deconvoluted PL curve by the total PL area); (b) CIE chromaticity diagram.

curves for all samples were composed of three PL components, corresponding to the region in the visible spectrum where the maximum peak intensity appears: a blue (maximum at 463 nm), a green (maximum at 533 nm), and a red (maximum at 612 nm) component. Each type of electron transition is represented by a different color and can be linked to a specific structural arrangement. The PeakFit deconvolution program was used to analyze the PL curve [37]. The observed high PL intensity seems to indicate that this material possesses an optimum structural order–disorder degree, resulting in photoluminescence that can be associated with different CIO NC defects generated during the synthesis process [38]. The white emission can be further characterized by the CIE (Commission Internationale de l'Éclairage 1931 chromaticity) coordinates for the emission spectrum of the CaIn_2O_4 NCs (Fig. 5b). The CIE coordinates for the CaIn_2O_4 NCs were $x = 0.3122$ and $y = 0.3821$. Liu et al. synthesized a $\text{CaIn}_2\text{O}_4:\text{Eu}^{3+}$ powder by the Pechini-type sol–gel process. In that study, under UV excitation (around 400 nm), the $\text{CaIn}_2\text{O}_4:1.0\% \text{Eu}^{3+}$ sample showed a strong white emission [39]. On the other hand, the results obtained herein indicated that pure CIO NC is a promising single-host white-light-emitting candidate for white LEDs.

To demonstrate the photocatalytic activity of the CIO NCs obtained by ultrasonic spray pyrolysis, photodegradation of MB was carried out in an aqueous dispersion (MB dye + CIO NCs catalyst) under UV light. The temporal evolution of the photocatalytic degradation of the aqueous MB dye solution is shown in Fig. 6.

The MB dye was totally photodegraded after 60 min under UV irradiation. Table 2 presents a comparison of the present results with those documented in the literature for the CaIn_2O_4 photocatalysts. As seen in Table 2, the photocatalytic efficiency of the powder suspensions of the CIO NCs for the photodegradation of MB under ultraviolet–visible irradiation was enhanced herein, with lower synthesis temperatures. Since the CaIn_2O_4 nanoparticles presented a spherical morphology, the surface area of the samples was determined to be approximately $23.88 \text{ m}^2 \text{ g}^{-1}$ based on the N_2 adsorption–desorption isotherms (Fig. S1-1). It is clear that the present CIO NCs are approximately 50% more efficient for photodegradation of MB than the best result presented in Table 2.

Tang et al. [15] reported that under visible photo-irradiation, MB degradation over the CIO photocatalyst involved direct photocatalytic decomposition over the CIO photocatalyst and photocatalytic conversion over CIO, assisted by the adsorbed MB dye.

Moreover, the primary factors that influence the photocatalytic

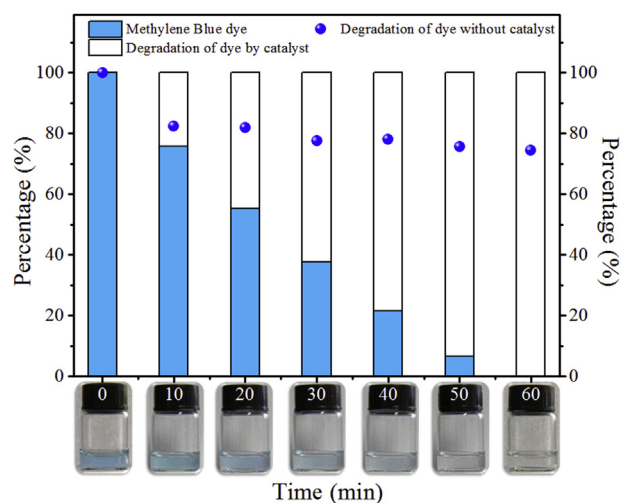


Fig. 6. Photodegradation efficiency of MB dye as a function of irradiation time for CIO NCs obtained by one-pot ultrasonic spray pyrolysis.

reaction are: (i) the adsorbability of the reactant on the catalyst surface; (ii) the absorptivity of the catalyst in the available light energy region; (iii) the efficient separation and transport of light-induced electrons and holes in the catalyst. For good adsorption of any reactant, a high catalyst surface area is desirable [10]. Hence, the better efficiency of the CIO NCs is related to the improved surface area, well-resolved spherical morphology, non-agglomerated particles with a narrow size distribution, and good crystallinity of the samples. Zhou et al. [40] reported that controlled interactions between light and matter could be achieved with a highly asymmetric structure. Researchers have shown that the growth of nanostructures may be tuned by controllable photolysis, resulting in an excellent ability to retain light over a wide range of wavelengths. These enhanced photon management capabilities make the material a promising candidate for application to optical detection. Thus, the light–matter interactions are of particular interest in the study of controllable photolysis-activated processes and various applications such as nanostructure-growth by heating and photocatalysis.

The newly designed CIO NCs were obtained by one-pot ultrasonic spray pyrolysis in one minute. The CIO NCs presented a

Table 2

Synthesis conditions, MB total photodegradation time, and surface area of CIO particles presented in the literature compared with the present data.

Material	Synthesis method	Synthesis/calcination time	MB photodegradation (min)	BET surface area ($\text{m}^2 \text{g}^{-1}$)	References
CaIn_2O_4	Solid-state reaction	24 h	120 (70% degradation)	1.23	[10]
CaIn_2O_4	Solid-state reaction	12 h	120	0.86	[11]
CaIn_2O_4	Solid-state reaction	12 h	120	0.86	[13]
CaIn_2O_4	Solution-combustion method	12 h	90	2.14	[15]
CaIn_2O_4	Ultrasonic spray pyrolysis	1 min	60	23.88	This work

uniformly distributed spherical morphology with an average size of 511 nm. In this study, the photocatalytic efficiency of the NCs towards the degradation of MB dye was compared with data reported in the literature for CIO obtained by different synthesis methods. The structural and morphological advantages of the CIO NCs resulted in better photocatalytic performance in comparison with previously reported species. Moreover, despite the short time required to obtain the CIO NCs, the samples presented good crystallinity and homogenous morphological characteristics. The present method provides a feasible approach for preparing shape- and size-controlled CIO NCs, which holds great potential for photocatalytic applications. Optical diffuse-reflectance UV–vis measurements of the CIO NCs were also performed. The optical band gap was estimated by using the Wood and Tauc equation [41]. The estimated optical band gap value was 3.82 eV (Fig. SI-2).

Fig. 7 shows the photodegradation of MB dye by the CIO NCs, where the temporal changes in the UV–vis absorbance spectra of the aqueous dye solutions were monitored. The degradation ratio (C_t/C_0) of the aqueous MB dye solutions was compared with that of different CaIn_2O_4 catalysts presented in the literature and with that achieved in the absence of a catalyst. Commercial TiO_2 -P25 was used as a standard catalyst. Fig. 7 indicates a significant reduction of the absorption maximum by around 95% for the MB aqueous solutions during the photodegradation process when CIO NCs were used as the catalyst. We assumed that a high percentage of the MB dye was photodegraded after 60 min under UV light. Moreover, it was verified herein, that the developed CIO NC catalyst obtained at 1223 K by ultrasonic spray pyrolysis was the most efficient for degradation of MB under UV irradiation relative to the catalysts described in the literature.

In the CIO NC superlattice, the inter-cluster (intermediary range) and intra-cluster (local range) interactions may be derived from

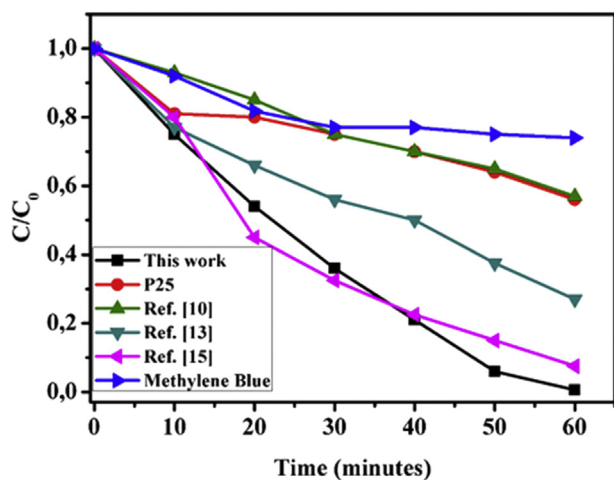


Fig. 7. Comparison of the photodegradation efficiency of MB as a function of irradiation time for different photocatalysts: standard catalyst P25, CIO NCs, and CIO described in the literature.

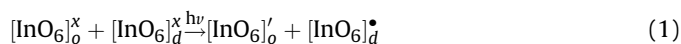
three different sources: orientation, induction, and dispersion interactions. The nanocrystals adopt cluster formations. The orientation interaction is associated with the correlation between the rotational motion of the permanent moments in different $[\text{InO}_6] - [\text{InO}_6]$, $[\text{CaO}_6] - [\text{CaO}_6]$, or $[\text{InO}_6] - [\text{CaO}_6]$ complex clusters (medium-range). The induction interaction occurs via polarization of $[\text{CaO}_6]$ or $[\text{InO}_6]$ clusters by the permanent moment of another neighbor, i.e., $[\text{InO}_6]$ or $[\text{CaO}_6]$ clusters (short-range). The dispersion interaction arises from the correlation between the electrons situated in the neighborhood of $[\text{InO}_6]$ or $[\text{CaO}_6]$ clusters (long-range). The effect of order–disorder in the nanocrystals and microspheres shows that a symmetry break occurs in the structure, and is a necessary condition for the existence of intermediary energy levels within the forbidden band gap. These structural changes are related to the charge polarization over the short and medium range, which may be a manifestation of quantum confinement (independently of the particle size). The key feature of quantum confinement is the presence of discrete energy levels within the band gap, which are not possible for a periodic crystal at long, medium, and short range.

The cluster-to-cluster charge transfer (CCCT) in a crystal containing more than one kind of cluster is characterized by excitations involving electronic transitions from one cluster to another. Longo et al. [27] demonstrated that the CCCT mechanism in hierarchical assemblies of CaIn_2O_4 ($[\text{InO}_6]_o - [\text{InO}_6]_d$ or $[\text{CaO}_6]_o - [\text{CaO}_6]_d$) can be considered a new class of electronic transitions involving electron–hole (e^-h^*) pairs. In this study, we propose that within the superlattice, the $[\text{InO}_6]_o$ or $[\text{CaO}_6]_o$ ordered clusters and the $[\text{InO}_6]_d$ or $[\text{CaO}_6]_d$ disordered clusters arise from structural distortions, where it is possible for electron transfer to occur between these species. Therefore, these $[\text{InO}_6]_o - [\text{InO}_6]_d$ and/or $[\text{CaO}_6]_o - [\text{CaO}_6]_d$ clusters present extrinsic defects, which are linked to the effects of order–disorder in the electronic structure, surfaces (nanocrystals), and interfaces (spheres). These defects create additional energy states above the valence band and below the conduction band, decreasing the band gap.

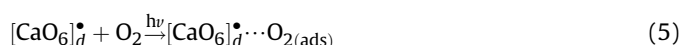
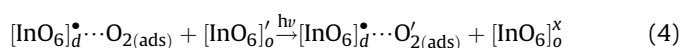
Structural and electronic reconstructions of all possible combinations of clusters belonging to a specific crystal are essential for understanding the CCCT process and its influence on the photocatalysis phenomenon. In the photo-induced charge-transfer process, the electrons are promoted from occupied levels of the donor clusters ($[\text{InO}_6]_d$ or $[\text{CaO}_6]_d$) to empty levels of the receptor clusters ($[\text{CaO}_6]_o$ or $[\text{InO}_6]_o$). The formation of isolated energy levels (quantum confinement) and the presence of disordered $[\text{InO}_6]_d$ and/or $[\text{CaO}_6]_d$ clusters cause substantial recombination between the photoexcited electron and hole during the photocatalysis processes.

In order to further explain the photocatalytic properties of the CIO NCs in one microsphere, the complex cluster model based on Kroger-Vink notation (1) was employed. This model predicts which intrinsic bulk defects (nanocrystals)/surface (microspheres) in the superlattice of the material are able to lead to polarization of the superlattice and indicates possible electronic transitions between disordered and ordered clusters that lead to the generation of e^-h^* pairs even before UV excitation. After UV illumination generation of

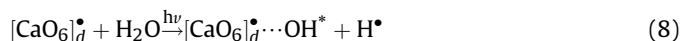
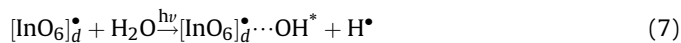
the $\dot{\epsilon}$ - h^{\bullet} pairs is intensified, leading to electronic transference within the band gap. Moreover, methylene blue is also excited.



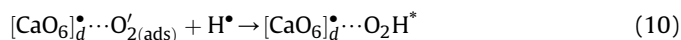
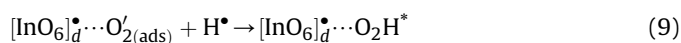
In the following stage, the generated $[\text{InO}_6]_o/[\text{InO}_6]_d$ and/or $[\text{CaO}_6]_o/[\text{CaO}_6]_d$ cluster complexes interact with the methylene blue, H_2O , and O_2 molecules until the dye is decolorized, as shown in Eqs. (3)–(6):



The clusters formed by the complex CIO cluster interact with water and separate it into hydroxyl radicals and hydrogen ions according to the following reactions:



The primary products of the partial oxidation reaction between water and the complex cluster, i.e., $[\text{InO}_6]_d^{\bullet}$ or $[\text{CaO}_6]_d^{\bullet}$, are hydroxyl radicals, OH^{\bullet} . These radicals exhibit high oxidation power and cause mineralization of organic compounds in water. The primary reaction is the formation of superoxide species $[\text{InO}_6]_d^{\bullet} \cdots \text{O}_2^{\bullet}$ or $[\text{CaO}_6]_d^{\bullet} \cdots \text{O}_2^{\bullet}$. These species then react with hydrogen ions (H^{\bullet}) and form a hydrogen peroxide radical ($\text{O}_2\text{H}^{\bullet}$) according to the following reactions:



The generated OH^{\bullet} and $\text{O}_2\text{H}^{\bullet}$ radicals are the main oxidizing species for the degradation of methylene blue. Moreover, it is possible that the generated $[\text{InO}_6]_o'/[\text{InO}_6]_d^{\bullet}$ and/or $[\text{CaO}_6]_o'/[\text{CaO}_6]_d^{\bullet}$ clusters affect the mechanism of photocatalysis, but are not active in the generation of $\dot{\epsilon}$ - h^{\bullet} pairs. In addition, adsorption of methylene blue on the semiconductor CIO NC surfaces plays an important role in the photocatalytic process.

Finally, it is noteworthy that it is still challenging to correlate the surface defects with the photocatalytic activity. A major problem is that the defects interact with many other factors and the photocatalytic activity of CIO may be dominated by defects existing in most of the CIO NCs with formation of spheres.

4. Conclusion

In summary, unique CIO NCs with predominantly spherical morphology were obtained by one-pot ultrasonic spray pyrolysis in one minute with good control of the synthesis parameters. The CIO NCs were characterized by X-ray diffraction, field-emission gun scanning electron microscopy, ultraviolet visible absorption

spectroscopy, and photoluminescence measurements. Powder suspensions of the CIO NCs exhibited enhanced photocatalytic efficiency for the photodegradation of methylene blue (MB) under ultraviolet–visible irradiation. The surface/bulk defects can influence the separation of photogenerated electron–hole pairs on the CIO NCs under irradiation and, therefore, influence the activity for the photocatalytic reaction.

The CIO microspheres presented a uniformly distributed spherical morphology with an average size of 511 nm. The photocatalytic efficiency of the CIO NCs for MB degradation was compared with that of previously reported CIO catalysts obtained by different synthesis methods. The structural and morphological advantages of the CIO NCs resulted in better photocatalytic performance than that of previously reported congeners. Moreover, despite the short time required to obtain the CIO NCs, the samples presented good crystallinity and homogenous morphological characteristics. The CIE coordinates calculated for the CIO NCs were $x = 0.31$ and $y = 0.38$; according to the CIE diagram, the values represent a point in the white region.

The present method provides a feasible approach for achieving shape- and size-controlled CIO NCs that hold great potential for photocatalytic applications and as photoluminescent materials capable of emitting white light.

Acknowledgment

The authors gratefully acknowledge the financial support of the Brazilian governmental research funding agencies CAPES, FAPESP 2013/07296-2, INCTMN 2008/57872-1, CNPq 402127/2013-7, and CNPq 573636/2008-7.

Appendix A. Supplementary data

Supplementary data related to this article can be found at <http://dx.doi.org/10.1016/j.jallcom.2015.10.155>.

References

- [1] S. Zhou, C. Li, G. Yang, G. Bi, B. Xu, Z. Hong, K. Miura, K. Hirao, J. Qiu, Self-limited nanocrystallization-mediated activation of semiconductor nanocrystal in an amorphous solid, *Adv. Funct. Mater.* 23 (2013) 5436–5443.
- [2] S. Zinatloo-Ajabshir, M. Salavati-Niasari, M. Hamadani, Praseodymium oxide nanostructures: novel solvent-less preparation, characterization and investigation of their optical and photocatalytic properties, *RSC Adv.* 5 (2015) 33792–33800.
- [3] S. Mortazavi-Derazkola, S. Zinatloo-Ajabshir, M. Salavati-Niasari, Novel simple solvent-less preparation, characterization and degradation of the cationic dye over holmium oxide ceramic nanostructures, *Ceram. Int.* 41 (2015) 9593–9601.
- [4] A.K. Batra, A.K. Chilvery, P. Guggilla, M. Aggarwal, J.R. Currie, Micro- and nano-structured metal oxides based chemical sensors: an overview, *J. Nanosci. Nanotechnol.* 14 (2014) 2065–2085.
- [5] K. Koumoto, R. Funahashi, E. Guilmeau, Y. Miyazaki, A. Weidenkaff, Y.F. Wang, C.L. Wan, Thermoelectric ceramics for energy harvesting, *J. Am. Ceram. Soc.* 96 (2013) 1–23.
- [6] A. Baszczuk, M. Jasiorski, M. Nyk, J. Hanuza, M. Maczka, W. Strek, Luminescence properties of europium activated SrIn_2O_4 , *J. Alloy Compd.* 394 (2005) 88–92.
- [7] W.K. Chang, D.S. Sun, H. Chan, P.T. Huang, W.S. Wu, C.H. Lin, Y.H. Tseng, Y.H. Cheng, C.C. Tseng, H.H. Chang, Visible light-responsive core-shell structured $\text{In}_2\text{O}_3/\text{CaIn}_2\text{O}_4$ photocatalyst with superior bactericidal properties and biocompatibility, *Nanomed. Nanotechnol.* 8 (2012) 609–617.
- [8] J. Ding, W. Yan, S. Sun, J. Bao, C. Gao, Fabrication of graphene/ CaIn_2O_4 composites with enhanced photocatalytic activity from water under visible light irradiation, *Int. J. Hydrog. Energy* 39 (2014) 119–126.
- [9] W. Yan, Y. Zhang, W. Xie, S. Sun, J. Ding, J. Bao, C. Gao, $\text{CaIn}_2\text{O}_4/\text{FeTiO}_3$ composite photocatalysts with enhanced visible light performance for hydrogen production, *J. Phys. Chem. C* 118 (2014) 6077–6083.
- [10] L. Ge, Preparation of novel visible-light-driven In_2O_3 - CaIn_2O_4 composite photocatalyst by sol-gel method, *J. Sol Gel Sci. Technol.* 44 (2007) 263–268.
- [11] B. Zheng, Q. Guo, D. Wang, H. Zhang, Y. Zhu, S. Zhou, energy-transfer modulation for enhanced photocatalytic activity of near-infrared upconversion photocatalyst, *J. Am. Ceram. Soc.* 98 (1) (2015) 136–140.

- [12] W.K. Chang, K. Koteswara Rao, H.C. Kuo, J.F. Cai, M.S. Wong, A novel core–shell like composite $\text{In}_2\text{O}_3/\text{CaIn}_2\text{O}_4$ for efficient degradation of methylene blue by visible light, *Appl. Catal. A Gen.* 321 (2007) 1–6.
- [13] J.W. Tang, Z.G. Zou, J.H. Ye, Kinetics of MB degradation and effect of pH on the photocatalytic activity of MIn_2O_4 ($M = \text{Ca}, \text{Sr}, \text{Ba}$) under visible light irradiation, *Res. Chem. Intermed.* 31 (2005) 513–519.
- [14] J.W. Tang, Z.G. Zou, M. Katagiri, T. Kako, J.H. Ye, Photocatalytic degradation of MB on MIn_2O_4 ($M = \text{alkali earth metal}$) under visible light: effects of crystal and electronic structure on the photocatalytic activity, *Catal. Today* 93–95 (2004) 885–889.
- [15] J.W. Tang, Z.G. Zou, J. Yin, J. Ye, Photocatalytic degradation of methylene blue on CaIn_2O_4 under visible light irradiation, *Chem. Phys. Lett.* 382 (2003) 175–179.
- [16] J. Tang, Z. Zou, J. Ye, Effects of substituting Sr^{2+} and Ba^{2+} for Ca^{2+} on the structural properties and photocatalytic behaviors of CaIn_2O_4 , *Chem. Mater.* 16 (2004) 1644–1649.
- [17] J. Ding, S. Sun, J. Bao, Z. Luo, C. Gao, Synthesis of CaIn_2O_4 rods and its photocatalytic performance under visible-light irradiation, *Catal. Lett.* 130 (2009) 147–153.
- [18] Y. Zhang, R. Selvaraj, M. Sillanpää, Y. Kim, C.W. Tai, Coprecipitates synthesis of CaIn_2O_4 and its photocatalytic degradation of methylene blue by visible light irradiation, *J. Ind. Eng. Chem.* 53 (2014) 11720–11726.
- [19] J. Sato, N. Saito, H. Nishiyama, Y. Inoue, Photocatalytic activity for water decomposition of indates with octahedrally coordinated D^{10} configuration. i. influences of preparation conditions on activity, *J. Phys. Chem. B* 107 (2003) 7965–7969.
- [20] X. Liu, R. Pang, Q. Li, J. Lin, Host-sensitized luminescence of Dy^{3+} , Pr^{3+} , Tb^{3+} in polycrystalline CaIn_2O_4 for field emission displays, *J. Solid State Chem.* 180 (2007) 1421–1430.
- [21] T. Li, C. Guo, H. Jiao, L. Li, D.K. Agrawal, Infrared-to-visible up-conversion luminescence of CaIn_2O_4 co-doped with $\text{RE}^{3+}/\text{Yb}^{3+}$ ($\text{RE} = \text{Tm}, \text{Pr}, \text{Nd}$), *Opt. Commun.* 312 (2014) 284–286.
- [22] T. Li, C.F. Guo, Y.M. Yang, L. Li, N. Zhang, Efficient green up-conversion emission in $\text{Yb}^{3+}/\text{Ho}^{3+}$ Co-doped CaIn_2O_4 , *Acta Mater.* 61 (2013) 7481–7487.
- [23] I. Taniguchi, Z. Bakenov, Spray pyrolysis synthesis of nanostructured $\text{LiFe}_{1-x}\text{Mn}_x\text{O}_4$ cathode materials for lithium-ion batteries, *Powder Technol.* 159 (2005) 55–62.
- [24] Y.J. Hong, M.Y. Son, B.K. Park, Y.C. Kang, One-pot synthesis of yolk–shell materials with single, binary, ternary, quaternary, and quinary systems, *Small* 9 (2013) 2224–2227.
- [25] I. Taniguchi, Powder properties of partially substituted $\text{LiM}_x\text{Mn}_{2-x}\text{O}_4$ ($M = \text{Al}, \text{Cr}, \text{Fe}$ and Co) synthesized by ultrasonic spray pyrolysis, *Mater. Chem. Phys.* 92 (2005) 172–179.
- [26] F.R. Cruickshank, D.M. Taylor, F.P. Glasser, Crystal chemistry of indates: calcium, cadmium, strontium and barium indates, *J. Inorg. Nucl. Chem.* 26 (1964) 937–941.
- [27] M.L. Moreira, J. Andres, J.A. Varela, E. Longo, Synthesis of fine micro-sized BaZrO_3 powders based on a decaoctahedron shape by the Microwave-Assisted Hydrothermal method, *Cryst. Growth Des.* 9 (2009) 833–839.
- [28] C. Liang, S. Huang, W. Zhao, W. Liu, J. Chen, H. Liu, Y. Tong, Polyhedral Fe_3O_4 nanoparticles for lithium ion storage, *New J. Chem.* 39 (2015) 2651–2656.
- [29] V.M. Longo, A.T. Figueiredo, A.B. Campos, J.W.M. Espinosa, A.C. Hernandez, C.A. Taft, J.R. Sambrano, J.A. Varela, E. Longo, Different origins of green-light photoluminescence emission in structurally ordered and disordered powders of calcium molybdate, *J. Phys. Chem. A* 112 (2008) 8920–8928.
- [30] V.M. Longo, L.S. Cavalcante, E.C. Paris, J.C. Sczancoski, P.S. Pizani, M.S. Li, J. Andres, E. Longo, J.A. Varela, Hierarchical assembly of CaMoO_4 nano-octahedrons and their photoluminescence properties, *J. Phys. Chem. C* 115 (2011) 5207–5219.
- [31] F.A. Kroger, H.J. Vink, Relation between the concentrations of imperfections in crystalline solids, *Solid State Phys.* 3 (1956) 307–435.
- [32] M. Mezhericher, A. Levy, I. Borde, Modelling the morphological evolution of nanosuspension droplet in constant-rate drying stage, *Chem. Eng. Sci.* 66 (2011) 884–896.
- [33] M. Mezhericher, T. Brosh, A. Levy, Modeling of particle pneumatic conveying using DEM and DPM methods, *Part. Sci. Technol.* 29 (2011) 197–208.
- [34] M. Farid, A new approach to modelling of single droplet drying, *Chem. Eng. Sci.* 58 (2003) 2985–2993.
- [35] M. Mezhericher, A. Levy, I. Borde, Modelling of particle breakage during drying, *Chem. Eng. Process.* 47 (2008) 1410–1417.
- [36] F.V. Motta, A.P.A. Marques, M.S. Li, M.F.C. Abreu, C.A. Paskocimas, M.R.D. Bomio, R.P. Souza, J.A. Varela, E. Longo, Preparation and photoluminescence characteristics of $\text{In}(\text{OH})_3 \cdot x\text{Tb}^{3+}$ obtained by Microwave-Assisted Hydrothermal method, *J. Alloy Compd.* 553 (2013) 338–342.
- [37] T. Ding, W.T. Zheng, H.W. Tian, J.F. Zang, Z.D. Zhao, S.S. Yu, X.T. Lia, F.L. Meng, Y.M. Wang, X.G. Kong, Temperature-dependent photoluminescence in $\text{La}_{2/3}\text{Ca}_{1/3}\text{MnO}_3$, *Solid State Commun.* 132 (12) (2004) 815–819.
- [38] J.C. Sczancoski, L.S. Cavalcante, M.R. Joya, J.A. Varela, P.S. Pizani, E. Longo, SrMoO_4 powders processed in microwave-hydrothermal: synthesis, characterization and optical properties, *Chem. Eng. J.* 140 (1) (2008) 632–637.
- [39] X. Liu, C. Lin, J. Lin, White light emission from Eu^{3+} in CaIn_2O_4 host lattices, *Appl. Phys. Lett.* 90 (8) (2007), 081904–3.
- [40] S. Zhou, T. Matsuoka, Y. Shimotsuma, M. Sakakura, M. Nishi, Z. Hong, J. Qiu, K. Hirao, K. Miura, Localized control of light–matter interactions by using nanoscale asymmetric TiO_2 , *Nanotechnology* 23 (2012) 465704.
- [41] D.L. Wood, J.S. Tauc, Weak absorption tails in amorphous semiconductors, *Phys. Rev.* 5 (1972) 3144–3151.